

# Anomalous Hall effect from gapped nodal line in $\text{Co}_2\text{FeGe}$ Heusler compound

Gaurav K. Shukla,<sup>1</sup> Jyotirmay Sau,<sup>2</sup> Nisha Shahi,<sup>1</sup> Anupam K. Singh,<sup>1</sup> Manoranjan Kumar,<sup>2</sup> and Sanjay Singh<sup>1</sup>

<sup>1</sup>*School of Materials Science and Technology, Indian Institute of Technology (Banaras Hindu University), Varanasi 221005, India*

<sup>2</sup>*S. N. Bose National Centre for Basic Sciences, Kolkata 700098, West Bengal, India*

Full Heusler compounds with Cobalt as a primary element show anomalous transport properties owing to the Weyl fermions and broken time-reversal symmetry. We present here the study of anomalous Hall effect (AHE) in  $\text{Co}_2\text{FeGe}$  Heusler compound. The experiment reveals anomalous Hall conductivity (AHC)  $\sim 100 \text{ S/cm}$  at room temperature with an intrinsic contribution of  $\sim 78 \text{ S/cm}$ . The analysis of anomalous Hall resistivity suggests the scattering independent intrinsic mechanism dominates the overall behaviour of anomalous Hall resistivity. The first principles calculation reveals that the Berry curvature originated by gapped nodal line near  $E_F$  is the main source of AHE in  $\text{Co}_2\text{FeGe}$  Heusler compound. The theoretically calculated AHC is in agreement with the experiment.

Weyl semimetals (WSMs) host exotic transport properties resulting from their non-trivial topological band structure [1–6]. WSMs are characterised by chiral anomaly and linear band crossing points known as Weyl points or Weyl nodes [7]. The existence of Weyl nodes are possible in metal or semimetal with broken inversion symmetry (IS) and/or time reversal symmetry (TRS). These broken symmetries lift the two fold degeneracy of electronic bands in the framework of Kramer’s theorem[8] and the linearly dispersing touching points of two non-degenerate bands become Weyl points [9, 10]. The Hamiltonian of the system describing Weyl nodes can be written in term of basis vector of three Pauli matrices and hence any perturbation with linear combination of Pauli matrices can not destroy the Weyl nodes [9]. Also no other symmetries require (except translational symmetry) for the protection of Weyl nodes that represent the Weyl nodes as topologically stable object [11]. Michel Berry introduced the concept of Berry curvature [12] which may be mapped to pseudo magnetic field and the degenerate Weyl points correspond to quantized monopoles form source and sink of Berry curvature. These concepts help us to understand the various intriguing phenomenon like anomalous Hall effect (AHE) [13, 14], anomalous Nernst effect (ANE) [15], chiral magnetoresistance [2, 7] and second harmonic generation [2] etc. Weyl points induced by the breaking of IS was observed experimentally first time in TaAs [16–18] and investigated extensively in its family members [19, 20] and also in other materials [21–23]. TRS breaking WSMs are also known as magnetic WSMs discovered very recently and created much interest due to exhibiting large intrinsic AHE and anomalous Hall conductivity (AHC) which is proportional to the separation of Weyl nodes [13, 24, 25]. The magnetic WSMs have added advantage over conventional WSMs because an external magnetic field can be used to manipulate the properties of magnetic WSMs [26].  $\text{Co}_3\text{SnS}_2$ , a ferromagnet kagome lattice is firstly discovered as magnetic WSM exhibits large Berry curvature resulting the giant intrinsic AHC  $1130 \text{ S/cm}$ , which is an order of magnitude larger than the typical ferromagnets[27]. This large Berry curvature attribute to the presence of Weyl nodes and nodal rings of

linear crossings in the spin-up channel based on band inversion. Besides,  $\text{Co}_3\text{SnS}_2$ , several other materials such as pyrochlore iridates [28–30],  $\text{PrAlGe}$  [26],  $\text{YMnBi}_2$  [31],  $\text{Mn}_3\text{Sn}$  [32],  $\text{Co}_3\text{MM}'\text{X}_2$  (  $\text{M}/\text{M}' = \text{Ge, Sn, Pb, X}=\text{S, Se, Te}$  ) [33] and Heusler alloys [24, 34–37] have been identified as magnetic WSMs theoretically and/or experimentally.

Among various magnetic WSM candidates,  $\text{Co}_2$  based Heusler compounds have been found to be more interesting that drives the large AHC due to a large Berry curvature [24, 34, 35, 38]. In most of the  $\text{Co}_2$  based magnetic WSMs, gapped nodal line in momentum space has been found as a major source of Berry curvature and creates intrinsic AHE [24, 39, 40]. In these compounds, three gapless nodal lines which are protected by three mirror planes exist in the absence of magnetization. The gapless nodal line gaps out with introduction of spin orbit coupling(SOC) according to the magnetization direction [13, 39]. For example,  $\text{Co}_2\text{MnGa}$  exhibits a giant AHC around  $1260 \text{ S/cm}$  at  $60 \text{ K}$  due to large Berry curvature associated with the gapped nodal line [40].  $\text{Co}_2\text{VGa}$  exhibit the AHC around  $140 \text{ S/cm}$  due to slight gapped nodal line result from reduced mirror symmetry upon introducing magnetization [15]. Recently,  $\text{Co}_2\text{MnAl}$  Weyl semimetal reported to have large AHC  $1600 \text{ S/cm}$  at  $2 \text{ K}$  due to gapped nodal ring in momentum space which is as large as for 3D quantum AHE [24].

Theoretical investigation performed on the  $\text{Co}_2\text{FeGe}$  Heusler compound reveals the existence of nodal line above the Fermi energy ( $E_F$ ) results in to an intrinsic AHE [14, 41]. In this manuscript, we present study of AHE on  $\text{Co}_2\text{FeGe}$  Heusler compound using both experiment and theoretical calculations. We found the experimental AHC  $\sim 100 \text{ S/cm}$  at  $300 \text{ K}$  and shows weak dependence on temperature. Our first principles calculation reveals that the magnetization induced gapped nodal line near the  $E_F$  is the main source of AHE in  $\text{Co}_2\text{FeGe}$ .

Polycrystalline  $\text{Co}_2\text{FeGe}$  compound was synthesized by standard arc melting technique [42] in the presence of pure argon atmosphere using 99.99% pure individual elements. The sample was remelted several times for the homogeneous mixing of involved elements. A small weight loss of  $0.62 \%$  was notified after melting. Small

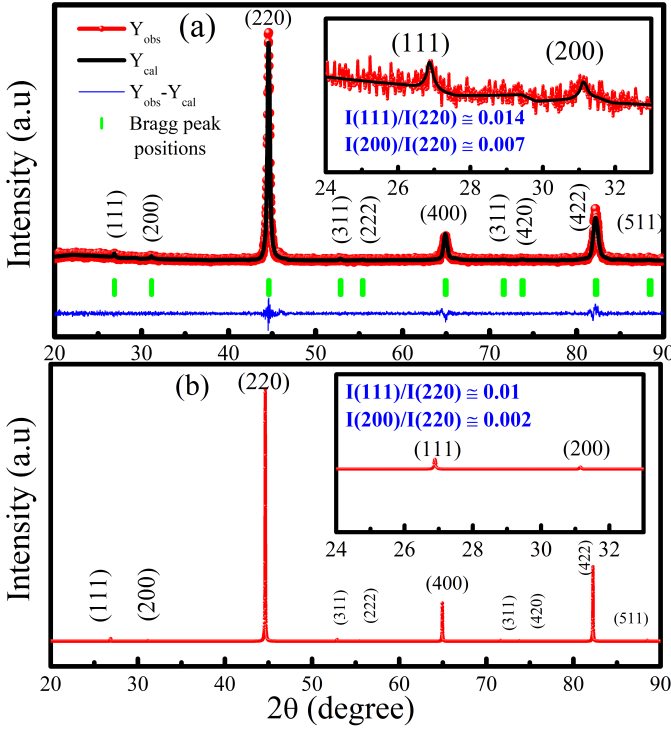


FIG. 1. (a) Rietveld modeling of X-ray diffraction pattern of  $\text{Co}_2\text{FeGe}$  at room temperature. (b) Simulated XRD pattern of  $\text{Co}_2\text{FeGe}$ . Inset of figures show the enlarged view around the (111) and (200) superlattice reflections.

piece was taken from sample and crushed into powder for X-ray diffraction measurement. The polished rectangular piece of the dimension  $4 \times 2 \times 0.65 \text{ mm}^3$  was used for temperature and magnetic field dependent transport measurements using cryogen free measurement system (Cryogenic, CFMS). To obtain the actual transverse resistivity ( $\rho_H$ ), raw Hall resistivity data ( $\rho_H^{\text{raw}}$ ) was anti-symmetrized by averaging the difference of  $\rho_H^{\text{raw}}$  at the positive field and negative field with respect to the field sweep direction.

The electronic band structure and magnetic properties of the  $\text{Co}_2\text{FeGe}$  are calculated employing density functional theory (DFT) using the Vienna-ab initio simulation package (VASP) [43]. Exchange-correlation potential is approximated with generalized gradient approximation and projector augmented wave method (PAW)[44] is used for core-valence interaction. The calculations are performed with K-mesh of  $10 \times 10 \times 10$  for the  $\text{Fm}\bar{3}\text{m}$  space group (space group no.225). The plane-wave basis is used with cut-off energy 500 eV and force convergence for the optimisation is kept below 0.001 eV/Å. Self-consistent calculations are performed to get the charge density and thereafter the band structure is calculated. To understand the DFT band structure, Wannier interpolated bands and corresponding tight-binding parameters are calculated using Wannier90 [45, 46]. The anomalous Hall conductivity (AHC), Berry curvature and energy gap for the given parameters are calculated using the WannierTool [47]. For

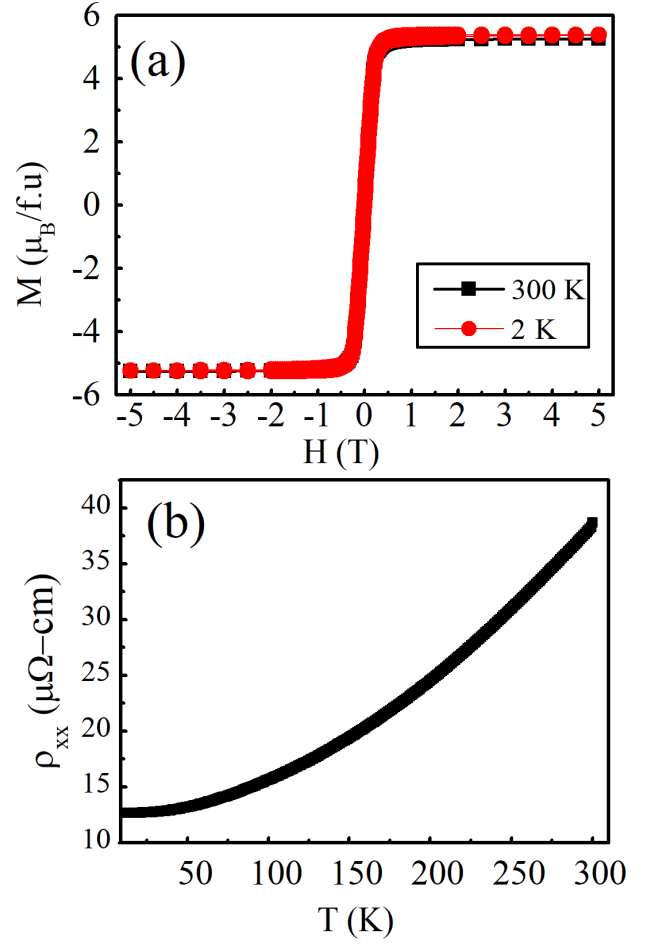


FIG. 2. (a) The field dependent magnetization curves at 2 K and 300 K. (b) Temperature dependent longitudinal resistivity  $\rho_{xx}$ .

AHC calculation Kubo formalism is used in the clean limit [48].  $\text{Co}_2\text{FeGe}$  material possess  $\text{Fm}\bar{3}\text{m}$  symmetry and have three relevant mirror planes  $m_x(k_x=0)$ ,  $m_y(k_y=0)$ ,  $m_z(k_z=0)$  and three  $C_4$  rotation axes  $k_x, k_y$  and  $k_z$  [49]. The magnetization is oriented along the z-axis and the SOC is also considered along the same axis.

X-ray diffraction (XRD) pattern of the sample collected at room temperature for structural investigation and phase purity. The Rietveld analysis of the XRD pattern was done using Fullprof software [50]. The space group  $\text{Fm}\bar{3}\text{m}$  and Wyckoff positions: 8c ( $1/4, 1/4, 1/4$ ) occupied by Co atoms, whereas 4b ( $1/2, 1/2, 1/2$ ) and 4a ( $0, 0, 0$ ) occupied by Fe and Ge atoms, respectively were used. The observed XRD patterns depicted in Fig.1a show that all the Bragg peaks observed are well indexed confirming the phase purity (cubic) of the  $\text{Co}_2\text{FeGe}$  sample. The refined unit cell parameter was found 5.74 Å.

For full Heusler alloys the reflections index relation  $h, k$  and  $l = \text{odd number}$  or  $(h+k+l)/2 = (2n+1)$  are the superlattice reflection, while  $(h+k+l)/2 = 2n$  are the fundamental reflections[51, 52]. The ordered structure of full Heusler alloys ( $\text{L}_{21}$  structure) generally mark the presence of (111) and (200) superlattice reflections; presence

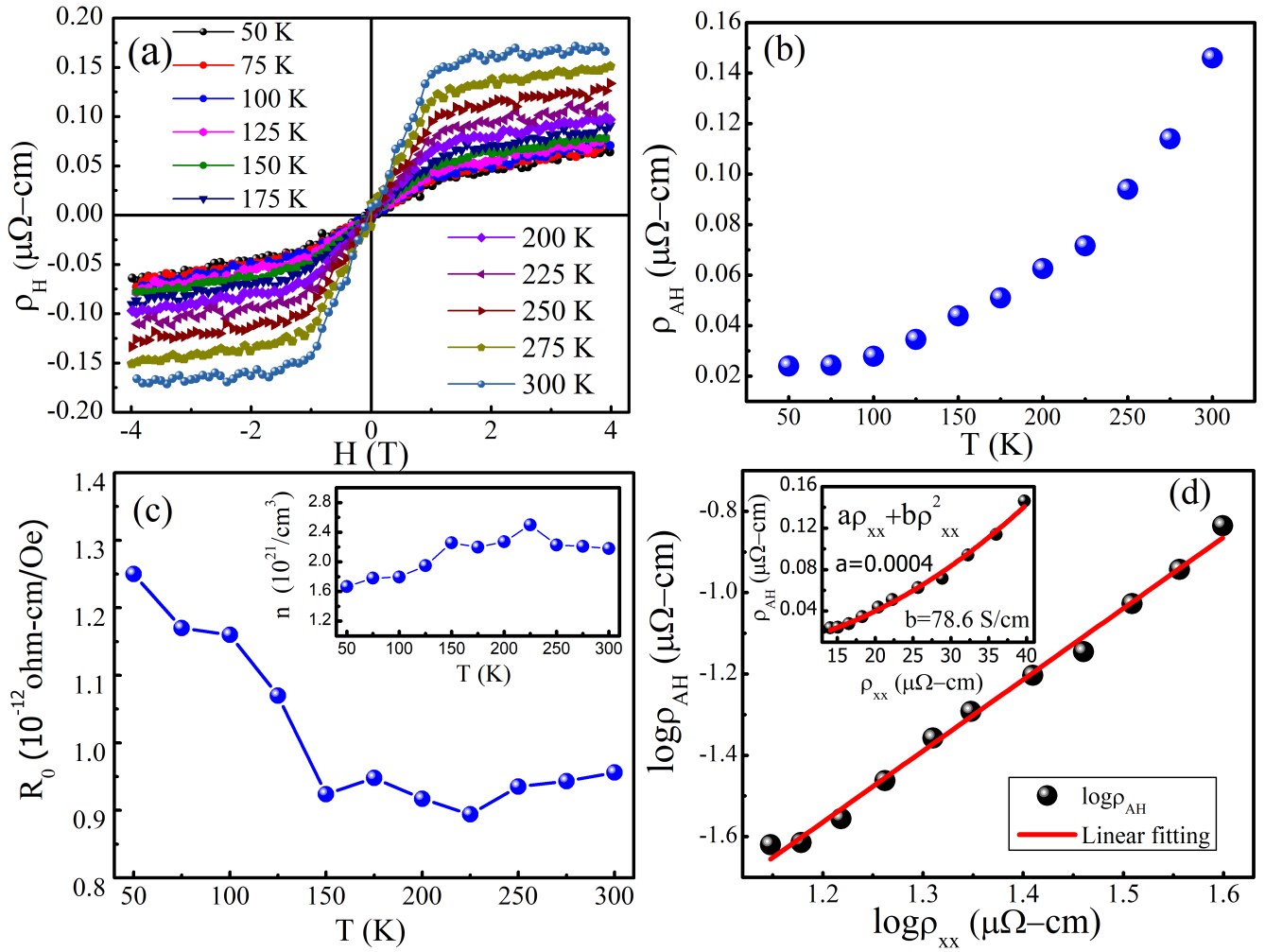


FIG. 3. (a) Field dependent Hall resistivity  $\rho_H$  at indicated temperatures. (b) Temperature dependent anomalous Hall resistivity  $\rho_{AH}$ . (c) Temperature dependent normal Hall coefficient  $R_0$ . Inset shows the temperature dependent carrier concentration  $n$ . (d) Double logarithmic plot between  $\rho_{AH}$  and  $\rho_{xx}$  (black balls) and linear fitting is shown by red line. Inset shows the graph between  $\rho_{AH}$  and  $\rho_{xx}$  (black balls) and fitting using Eq.(1) is shown by red line.

of (111) peak indicates the chemical ordering of atom at the octahedral position, and (200) peak indicates the ordering at the tetrahedral position, while the intensity of (220) fundamental reflection is independent from atomic ordering [53]. The presence of both (111) and (200) superlattice peaks primarily suggest the  $L2_1$  structure of  $\text{Co}_2\text{FeGe}$  as shown in inset of Fig.1a. To compare the experimentally observed relative intensities of the superlattice reflections with theory, we simulated the XRD pattern using PowderCell software as shown in Fig.1b. Similar to the observed, weak intensities of (111) and (200) superlattice reflections have also been observed in simulated XRD pattern. The enlarged view of simulated superlattice peaks are shown in the inset of Fig.1b. The weak intensity of superlattice reflections is due to the small difference between atomic scattering factor of constituent 3d metals of  $\text{Co}_2\text{FeGe}$  [54, 55]. The measured and simulated  $\frac{I_{111}}{I_{220}}$  and  $\frac{I_{200}}{I_{220}}$  are given in inset of Fig.1a and Fig.1b respectively. A good match between the measured and simulated XRD pattern suggests the formation

of ordered structure of  $\text{Co}_2\text{FeGe}$ .

Magnetic isotherms up to field of 5 Tesla were recorded at temperatures 2 K and 300 K depicted in Fig.2a. The magnetic moment was found to be  $5.38 \mu_B/\text{f.u}$  and  $5.24 \mu_B/\text{f.u}$  at 2 K and 300 K, respectively. The observed magnetic moment is well agreement with the literature [56, 57] as well as our theoretical calculation (discussed later). The variation of longitudinal resistivity ( $\rho_{xx}$ ) as a function of temperature from 10 K to 300 K is shown in Fig.2b. The  $\rho_{xx}$  increases with increasing temperature and a residual resistivity about  $14 \mu\Omega\text{cm}$  is observed. The non-linear behaviour of resistivity above 50 K suggests the combined phonon and magnon scattering state [58]. The residual resistance ratio (RRR= $\rho_{xx}(300\text{K})/\rho_{xx}(10\text{K})$ ) which quantifies the degree of disorder is 2.82. This value is larger than the most of  $\text{Co}_2$ -based Heusler alloy [39, 59–62] signifies comparatively clean sample.

After investigation of the phase purity, saturation magnetization and temperature variation of the longitudinal

resistivity, we carried out a detailed magneto-transport measurement in a wide range of temperature 50 K to 300 K to study the AHE in the  $\text{Co}_2\text{FeGe}$  Heusler alloy. Hall resistivity ( $\rho_H$ ) curves measured up to 4 Tesla magnetic field at different temperatures are shown in Fig.3a. The  $\rho_H$  is given by equation  $\rho_H(H) = R_0H + R_sM$  [39, 63]. Where  $R_0$  and  $R_s$  are the normal and anomalous Hall coefficients.  $H$  is the external applied magnetic field and  $M$  is magnetization of the material. It is evident from Fig.3a that  $\rho_H$  initially increases at lower fields indicating AHE in  $\text{Co}_2\text{FeGe}$  and shows the positive slope according to sign of ordinary Hall coefficient at higher field region for all temperatures. The anomalous Hall resistivity ( $\rho_{AH}$ ) calculated by the zero field extrapolation of high field Hall data with the ordinate, which is equivalent to Hall voltage response arising due to spontaneous magnetization in the absence of external magnetic field. Fig.3b, shows the extracted  $\rho_{AH}$  versus temperature plot, which displays that the Hall resistivity increases with increasing temperature and acquire a maximum value of  $0.14\mu\Omega\text{-cm}$  at room temperature and a small value  $0.02\mu\Omega\text{-cm}$  at 50K. The slope of high field Hall resistivity data gives the normal Hall coefficient ( $R_0$ ) and variation of  $R_0$  with temperature is shown in Fig 3c. By using relation  $R_0 = \frac{1}{ne}$ , we calculated carrier density ( $n$ ) and plotted in the inset of Fig.3 (c) with temperature. The value of  $n$  was found  $\sim 2 \times 10^{21}/\text{cm}^3$ . The positive value of  $R_0$  indicates that the holes are majority charge carriers in the whole temperature range.

In order to investigate the origin of AHE, we analysed the  $\rho_{AH}$  versus  $\rho_{xx}$  on a double logarithmic scale. A linear fitting was employed to determine the exponent  $\beta$  according to the scaling relation  $\rho_{AH} \propto \rho_{xx}^\beta$  [62, 64] shown in Fig.3(d). The exponent  $\beta$  decides the dependency of  $\rho_{AH}$  on  $\rho_{xx}$ . According to well established theory of AHE,  $\beta = 1$  is for the AHE originates from the skew scattering mechanism and  $\beta = 2$  is for the AHE govern by scattering independent mechanism [65]. By this procedure, we found the exponent  $\beta = 1.75$ , which indicates the Berry phase mechanism as dominant contribution in AHE. To find the value of intrinsic AHC, we have plotted  $\rho_{AH}$  versus  $\rho_{xx}$  (Inset of Fig.3d) and fitted with equation

$$\rho_{AH} = a\rho_{xx} + b\rho_{xx}^2 \quad (1)$$

Here  $a$  and  $b$  are the skew scattering coefficient and intrinsic AHC, respectively. By this, we found  $a = 0.0004$  and intrinsic AHC  $b \sim 78 \text{ S/cm}$ . The AHC due to extrinsic side jump contribution usually order of  $e^2/hc(\epsilon_{\text{SOC}}/E_F)$ , where  $\epsilon_{\text{SOC}}$  and  $E_F$  are the spin-orbit interaction energy and Fermi energy respectively [66]. For metallic ferromagnets  $\epsilon_{\text{SOC}}/E_F$  is generally less than  $10^{-2}$  [62, 67] and hence the side jump contribution in AHC is too small or negligible in comparison to intrinsic AHC. Further, to understand the microscopic origin of AHE, we need to look towards the variation of AHC with temperature and/or longitudinal resistivity. For this, we calculated Hall conductivity using tensor conversion for-

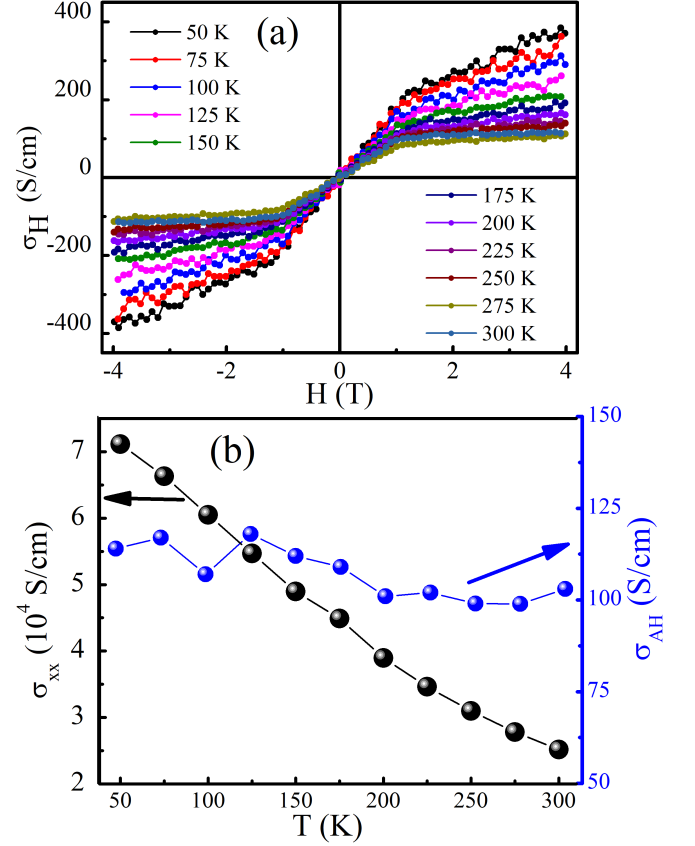


FIG. 4. (a) Field dependent Hall conductivity  $\sigma_H$  (b) Temperature dependent longitudinal conductivity  $\sigma_{xx}$  (black spheres) and AHC (blue spheres).

mula

$$\sigma_H = \frac{\rho_H}{(\rho_{xx}^2 + \rho_H^2)} \quad (2)$$

Fig.4a displays the field dependent Hall conductivity curves at indicated temperatures. The AHC was calculated by zero field extrapolation of high field Hall conductivity data on y axis and found close to  $100 \text{ S/cm}$  at room temperature. Fig.4b shows variation of longitudinal conductivity and AHC with temperature. AHC is nearly insensitive to temperature from several K to 300K, while the longitudinal resistivity shows explicit temperature dependence, fairly indicates the origin of AHE governed by the intrinsic mechanism [64, 68, 69]. Since the intrinsic AHE merely depends on the band structure of material so to get a better understanding of the origin of intrinsic AHE, we carried out first principles calculation on  $\text{Co}_2\text{FeGe}$ .

Our ab-initio calculation for a magnetic moment suggests that Fe and Co have a large magnetic moment with  $\mu_{Fe} = 2.84 \mu_B/\text{f.u}$  and  $\mu_{Co} = 1.34 \mu_B/\text{f.u}$  respectively, whereas Ge has a small vanishing magnetic moment. The total magnetic moment per formula unit is  $5.53 \mu_B$ , aligned along the (001) direction and the d-orbital of the transition atoms Fe and Co are the major contributors. The magnetic moment of full Heusler alloys generally follow

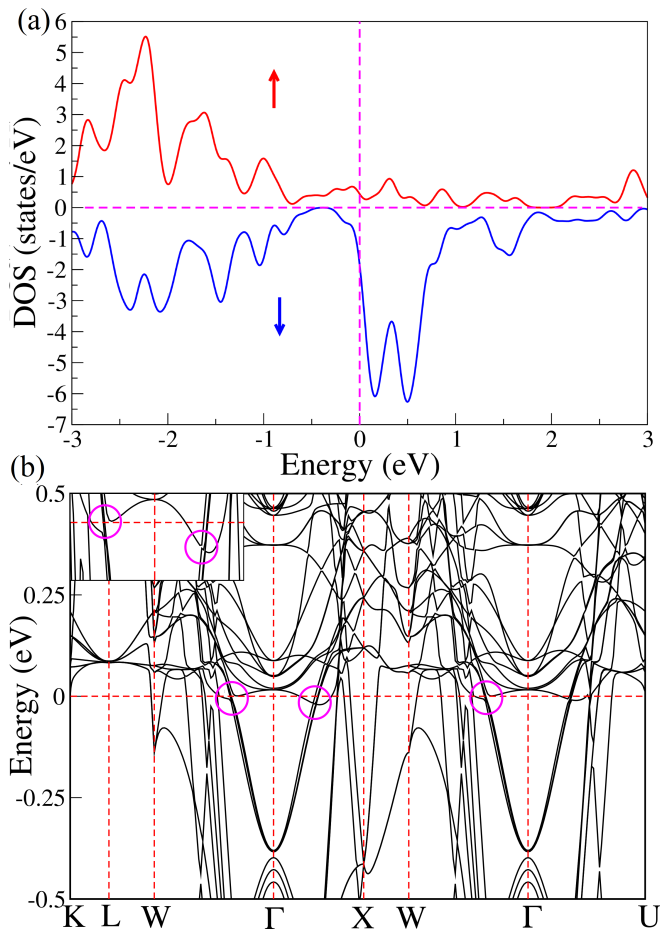


FIG. 5. (a) The total density of state (DOS) of  $\text{Co}_2\text{FeGe}$  for on site Coulomb interaction  $U=0$ . Red and blue curves represent the total DOS for majority and minority spins. (b) The band structure of  $\text{Co}_2\text{FeGe}$  in the presence of SOC (gapped nodal lines are shown in circle and inset shows the enlarged view around gapped nodal line).

low the Slater Pauling (SP) rule[70];  $M = Z - 24$ , where  $M$  and  $Z$  are magnetic moments and number of valance electrons, if the  $E_F$  lies in the band gap of the minority spin states. For  $\text{Co}_2\text{FeGe}$ , as per SP rule the total magnetic moment should be  $6 \mu_B/\text{f.u.}$ . In some cases these systems may have gapless minority bands or minority bands crossing the  $E_F$ , then a small deviation in total magnetic moment from the SP rule may be expected [70]. The calculated magnetic moment for  $\text{Co}_2\text{FeGe}$  is in well agreement with the experimental value ( $5.38 \mu_B/\text{f.u.}$ ), but this value is smaller than the predicted by the SP rule. To understand the deviation of magnetic moment total density of state(DOS) is calculated and shown in Fig.5a. Total DOS of minority spin electrons have finite value at  $E_F$ , which indicates presence of gapless states at the  $E_F$  or bands crossing  $E_F$ . Similar finite value of total DOS at  $E_F$  is also reported in literature for onsite Coulomb interaction  $U = 0$  [56, 71, 72]. We also performed calculations considering onsite Coulomb repulsion  $U$ ; 1.92 and 1.8 for the Co and Fe, respectively [73] and the calculated value of magnetic moment is  $\approx 6.00 \mu_B/\text{f.u.}$ , which overesti-

mates relative to experimental value, however, the magnetic moment is in agreement with literature [55, 56, 72]. Therefore, we believe that  $U = 0$  is more suitable parameter to explain the experimental findings. Similar conclusion is also reported for other  $\text{Co}_2$ -based Heusler alloys [35, 74].

This material is expected to show nodal line due to three relevant mirror planes  $m_x(k_x=0), m_y(k_y=0), m_z(k_z=0)$  in absence of SOC[41]. In presence of SOC the nodal lines will gap out according to the magnetization direction and introduce Berry curvature in the system [13, 41]. To understand the topological aspects, the nodal lines in the electronic band structure are analysed in absence and presence of SOC. The band structure with SOC coupling is calculated from the DFT calculation shown in Fig.5b. The band crossings are gaped out just below or at the  $E_F$  due to perturbation of SOC and these tiny gaps are shown inside the circle.

We analyzed the spectrum of tight binding model Hamiltonian calculated from the Wannier90 [45, 46] calculation with the help of Wanniertool [47]. In Fig.6a and Fig.6b, we have shown energy gap between the lowest conduction band and the topmost valence band at  $k_x=0$  plane and gaps are shown on a logarithmic scale of color plot in absence as well as in the presence of SOC, respectively. The gaps smaller than  $10^{-4}$  eV are considered to be gapless. We noticed that four semi-circular nodal lines appear in  $k_y - k_z$  plane of first Brillouin zone (Fig.6a) and in the presence of the SOC, the gapless semi-circular nodal lines are gaped out (Fig.6b). This material shows an intrinsic AHC, which can be expressed within the framework of linear response theory of the Kubo formalism[48];

$$\sigma_{\alpha\beta} = -\frac{e^2}{\hbar} \sum_n \int \frac{d^3k}{(2\pi)^3} \Omega_{\alpha\beta}^n(k) f_n(k) \quad (3)$$

where Berry curvature  $\Omega$  can be written as a sum over eigenstates[75].

$$\Omega_{\alpha\beta}^n = i \sum_{n \neq n'} \frac{\langle n | \frac{\partial H}{\partial R^\alpha} | n' \rangle \langle n' | \frac{\partial H}{\partial R^\beta} | n \rangle - (\alpha \leftrightarrow \beta)}{(\epsilon_n - \epsilon_{n'})^2} \quad (4)$$

Here  $|n\rangle, \epsilon_n$  and  $\epsilon_{n'}$  are the energy eigenstate and eigenvalue of  $n$  and  $n'$  bands respectively.  $H, f_n$  and  $\Omega_{\alpha\beta}^n$  are the Hamiltonian, Fermi distribution function and Berry curvature respectively. The  $\Omega_{\alpha\beta}^n$  is related to the change of electronic wave-function within the Brillouin zone. The detail of Berry curvature is in the appendix.

In Fig.6d, local Berry curvature is shown in  $k_x = 0$  plane of Brillouin zone. Intrinsic AHC is calculated using maximally localized Wannier orbitals using  $101 \times 101 \times 101$  k grid. The intrinsic AHC is proportional to the Brillouin zone summation of the Berry curvature over all occupied states and can be calculated using Eq.(3). We notice that the major contribution of AHC comes from neighborhood of nodal lines. The AHC as a function of  $E - E_F$  is shown in Fig.6c. The calculated AHC value

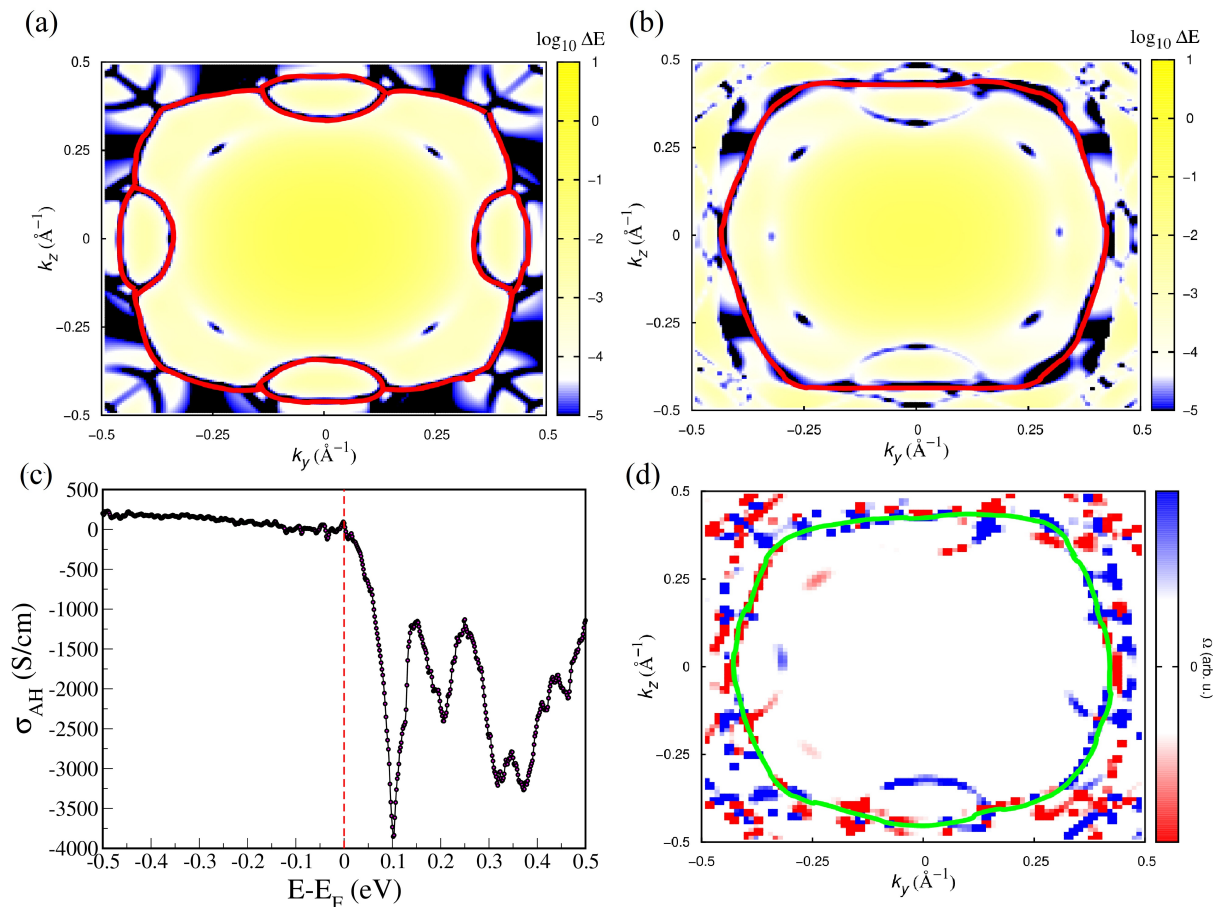


FIG. 6. Energy gap  $\Delta E(k_y, k_z)$  is plotted in  $k_y$ - $k_z$  plane at  $k_x = 0$  (a) without SOC (b) with SOC. Solid red lines represent gapless regions. (c) Energy ( $E - E_F$ ) dependence of the AHC. (d) Berry curvature distribution in  $k_y$ - $k_z$  plane at  $k_x = 0$ . Solid red lines represent gapless regions.

at  $E_F$  is found 77.29 S/cm, which well matches with the experimentally found intrinsic AHC 78.6 S/cm. We have also calculated the energy dependent AHC as shown in Fig.6c and it is evident that Fermi level shift in  $\text{Co}_2\text{FeGe}$  will result into an increased AHC.

In conclusion, we have experimentally investigated the AHE in  $\text{Co}_2\text{FeGe}$  Heusler alloy and performed first principle calculations to understand the origin of intrinsic AHE. Experimentally AHC was found close to 100 S/cm at 300 K with an intrinsic contribution of 78.6 S/cm. Berry curvature calculations give AHC about 77.29 S/cm due to magnetization induced gapped nodal line near the  $E_F$ , which is in well agreement with the experimentally calculated intrinsic AHC.

SS thanks Science and Engineering Research Board of India for financial support through the award of Ramanujan Fellowship (grant no: SB/S2/RJN-015/2017) and Early Career Research Award (grant no: ECR/2017/003186) for financial support. GKS thanks DST-INSPIRE scheme for fellowship. MK thanks DST for funding through grant no. CRG/2020/000754.

## Appendix

In the semi-classical limit, electrons moving in bands of the magnetic system require additional terms for the anomalous contribution to the conductivity and correction is done considering the wave packet rather than just particle movement [48]. Wave packet can be written as

$$W_{k_c, \mathbf{r}_c}(\mathbf{r}, t) = \sum_k a_k(k_c, t) \psi_{nk}(\mathbf{r}) \quad (\text{A.1})$$

where,  $\psi_{nk}(\mathbf{r} = e^{i\mathbf{k}\cdot\mathbf{r}} u_n(\mathbf{r}, k)$ . A wave packet is strongly centered at  $k_c$  in the Brillouin zone.  $\mathbf{r}_c$  is the spatial center position of a wave packet. Here,  $\mathbf{r}_c$  is defined by-

$$\mathbf{r}_c = \langle W_{k_c, \mathbf{r}_c} | \mathbf{r} | W_{k_c, \mathbf{r}_c} \rangle \quad (\text{A.2})$$

and  $a_k(k_c, t)$ , the phase of the weighting function can be given as

$$a_k(k_c, t) = |a_k(k_c, t)| e^{i(k-k_c)\cdot\mathbf{A}_n(k_c) - ik\cdot\mathbf{r}_c} \quad (\text{A.3})$$

$$\mathbf{A}_n(k_c) = i \int_{u.c.} \mathbf{d}^3r u_n^*(\mathbf{r}, k_c) \nabla_k u_n(\mathbf{r}, k_c) \quad (\text{A.4})$$

$\mathbf{A}_n(k_c)$  is the Berry connection. Using the wave packet of equation, one can write the Lagrangian and thereafter anomalous velocity can be calculated solving the Lagrangian. Anomalous velocity can be given as [48]

$$v_n = \frac{e}{\hbar} E \times \Omega_n(k_c) \quad (\text{A.5})$$

where  $E$  is an electric field and  $\Omega_n(k_c)$  is Berry curvature. The Berry curvature of a solid-state material in tight binding limit can be written as  $\Omega_n(k) = \Omega_n^k(k) + \Omega_n^r(k)$ . For non-degenerate energy bands, these are defined as

$$\Omega_n^k(k) = -i \sum_{m \neq n} \left[ \frac{C_n^\dagger(k) \nabla_k H(k) C_m(k)}{(\epsilon_{nk} - \epsilon_{mk})^2} \times C_m^\dagger(k) \nabla_k H(k) C_n(k) \right] \quad (\text{A.6})$$

$$\Omega_n^r(k) = \sum_{m \neq n} 2Re \left[ \frac{C_n^\dagger(k) \nabla_k H(k) C_m(k)}{(\epsilon_{nk} - \epsilon_{mk})} \times C_m^\dagger(k) \mathbf{r} C_n(k) \right] \quad (\text{A.7})$$

Where  $\epsilon_{nk}$  and  $C_k^n$  are energy of  $n^{\text{th}}$  band and coefficient of wave function respectively.  $H(k)$  is a Hamiltonian. However, for the degenerate band, the  $\Omega_n(k_c)$  can be calculated as in equations 73 and 74 of ref [48].

- 
- [1] S. Wang, B.-C. Lin, A.-Q. Wang, D.-P. Yu, and Z.-M. Liao, Quantum transport in Dirac and Weyl semimetals: A review, *Advances in Physics: X* **2**, 518 (2017).
- [2] N. Nagaosa, T. Morimoto, and Y. Tokura, Transport, magnetic and optical properties of Weyl materials, *Nature Reviews Materials* **5**, 621 (2020).
- [3] B. Yan and C. Felser, Topological materials: Weyl semimetals, *Annual Review of Condensed Matter Physics* **8**, 337 (2017).
- [4] D. Hsieh, Y. Xia, L. Wray, D. Qian, A. Pal, J. Dil, J. Osterwalder, F. Meier, G. Bihlmayer, C. Kane, *et al.*, Observation of unconventional quantum spin textures in topological insulators, *Science* **323**, 919 (2009).
- [5] J.-L. Xu, Y.-J. Sun, J.-L. He, Y. Wang, Z.-J. Zhu, Z.-Y. You, J.-F. Li, M. M. Chou, C.-K. Lee, and C.-Y. Tu, Ultrasensitive nonlinear absorption response of large-size topological insulator and application in low-threshold bulk pulsed lasers, *Scientific reports* **5**, 1 (2015).
- [6] P. Hosur and X. Qi, Recent developments in transport phenomena in Weyl semimetals, *Comptes Rendus Physique* **14**, 857 (2013).
- [7] B. Lv, T. Qian, and H. Ding, Experimental perspective on three-dimensional topological semimetals, *Reviews of Modern Physics* **93**, 025002 (2021).
- [8] M. J. Klein, On a degeneracy theorem of kramers, *American Journal of Physics* **20**, 65 (1952).
- [9] T. Chen, T. Tomita, S. Minami, M. Fu, T. Koretsune, M. Kitatani, I. Muhammad, D. Nishio-Hamane, R. Ishii, F. Ishii, *et al.*, Anomalous transport due to Weyl fermions in the chiral antiferromagnets  $\text{Mn}_3\text{X}$ , ( $\text{X} = \text{Sn}, \text{Ge}$ ), *Nature Communications* **12**, 1 (2021).
- [10] A. Burkov, Topological semimetals, *Nature materials* **15**, 1145 (2016).
- [11] S. A. Yang, Dirac and Weyl materials: fundamental aspects and some spintronics applications, in *Spin*, Vol. 6 (World Scientific, 2016) p. 1640003.
- [12] M. V. Berry, Quantal phase factors accompanying adiabatic changes, *Proceedings of the Royal Society of London. A. Mathematical and Physical Sciences* **392**, 45 (1984).
- [13] K. Manna, Y. Sun, L. Muechler, J. Kübler, and C. Felser, Heusler, Weyl and Berry, *Nature Reviews Materials* **3**, 244 (2018).
- [14] J. Noky, J. Gooth, C. Felser, and Y. Sun, Characterization of topological band structures away from the Fermi level by the anomalous Nernst effect, *Physical Review B* **98**, 241106 (2018).
- [15] K. Manna, L. Muechler, T.-H. Kao, R. Stinchhoff, Y. Zhang, J. Gooth, N. Kumar, G. Kreiner, K. Koepf, R. Car, *et al.*, From colossal to zero: controlling the anomalous Hall effect in magnetic Heusler compounds via Heusler curvature design, *Physical Review X* **8**, 041045 (2018).
- [16] S.-Y. Xu, I. Belopolski, N. Alidoust, M. Neupane, G. Bian, C. Zhang, R. Sankar, G. Chang, Z. Yuan, C.-C. Lee, *et al.*, Discovery of a Weyl fermion semimetal and topological Fermi arcs, *Science* **349**, 613 (2015).
- [17] L. Yang, Z. Liu, Y. Sun, H. Peng, H. Yang, T. Zhang, B. Zhou, Y. Zhang, Y. Guo, M. Rahn, *et al.*, Weyl semimetal phase in the non-centrosymmetric compound TaAs, *Nature physics* **11**, 728 (2015).
- [18] B. Lv, N. Xu, H. Weng, J. Ma, P. Richard, X. Huang, L. Zhao, G. Chen, C. Matt, F. Bisti, *et al.*, Observation of Weyl nodes in TaAs, *Nature Physics* **11**, 724 (2015).
- [19] Y. Sun, Y. Zhang, C. Felser, and B. Yan, Strong intrinsic spin Hall effect in the TaAs family of Weyl semimetals, *Phys. Rev. Lett.* **117**, 146403 (2016).
- [20] S.-Y. Xu, I. Belopolski, D. S. Sanchez, C. Zhang, G. Chang, C. Guo, G. Bian, Z. Yuan, H. Lu, T.-R. Chang, *et al.*, Experimental discovery of a topological Weyl semimetal state in TaP, *Science advances* **1**, e1501092 (2015).
- [21] A. A. Soluyanov, D. Gresch, Z. Wang, Q. Wu, M. Troyer, X. Dai, and B. A. Bernevig, Type-II Weyl semimetals, *Nature* **527**, 495 (2015).
- [22] Y. Sun, S.-C. Wu, M. N. Ali, C. Felser, and B. Yan, Prediction of Weyl semimetal in orthorhombic  $\text{MoTe}_2$ , *Physical Review B* **92**, 161107 (2015).
- [23] J. Liu and D. Vanderbilt, Weyl semimetals from noncentrosymmetric topological insulators, *Physical Review B* **90**, 155316 (2014).
- [24] P. Li, J. Koo, W. Ning, J. Li, L. Miao, L. Min, Y. Zhu,

- Y. Wang, N. Alem, C.-X. Liu, *et al.*, Giant room temperature anomalous Hall effect and tunable topology in a ferromagnetic topological semimetal  $\text{Co}_2\text{MnAl}$ , *Nature communications* **11**, 1 (2020).
- [25] A. Zyuzin, S. Wu, and A. Burkov, Weyl semimetal with broken time reversal and inversion symmetries, *Physical Review B* **85**, 165110 (2012).
- [26] D. Destraz, L. Das, S. S. Tsirkin, Y. Xu, T. Neupert, J. Chang, A. Schilling, A. G. Grushin, J. Kohlbrecher, L. Keller, *et al.*, Magnetism and anomalous transport in the Weyl semimetal  $\text{PrAlGe}$ : possible route to axial gauge fields, *npj Quantum Materials* **5**, 1 (2020).
- [27] E. Liu, Y. Sun, N. Kumar, L. Muechler, A. Sun, L. Jiao, S.-Y. Yang, D. Liu, A. Liang, Q. Xu, *et al.*, Giant anomalous Hall effect in a ferromagnetic kagome-lattice semimetal, *Nature physics* **14**, 1125 (2018).
- [28] X. Wan, A. M. Turner, A. Vishwanath, and S. Y. Savrasov, Topological semimetal and Fermi arc surface states in the electronic structure of pyrochlore iridates, *Physical Review B* **83**, 205101 (2011).
- [29] K. Ueda, R. Kaneko, H. Ishizuka, J. Fujioka, N. Nagaosa, and Y. Tokura, Spontaneous Hall effect in the Weyl semimetal candidate of all-in all-out pyrochlore iridate, *Nature communications* **9**, 1 (2018).
- [30] K. S. Takahashi, H. Ishizuka, T. Murata, Q. Y. Wang, Y. Tokura, N. Nagaosa, and M. Kawasaki, Anomalous Hall effect derived from multiple Weyl nodes in high-mobility  $\text{EuTiO}_3$  films, *Science advances* **4**, eaar7880 (2018).
- [31] S. Borisenko, D. Evtushinsky, Q. Gibson, A. Yaresko, K. Koepnik, T. Kim, M. Ali, J. van den Brink, M. Hoesch, A. Fedorov, *et al.*, Time-reversal symmetry breaking type-II Weyl state in  $\text{YbMnBi}_2$ , *Nature communications* **10**, 1 (2019).
- [32] K. Kuroda, T. Tomita, M.-T. Suzuki, C. Bareille, A. Nugroho, P. Goswami, M. Ochi, M. Ikhlas, M. Nakayama, S. Akebi, *et al.*, Evidence for magnetic Weyl fermions in a correlated metal, *Nature materials* **16**, 1090 (2017).
- [33] W. Luo, Y. Nakamura, J. Park, and M. Yoon, Cobalt-based magnetic Weyl semimetals with high-thermodynamic stabilities, *npj Computational Materials* **7**, 1 (2021).
- [34] I. Belopolski, K. Manna, D. S. Sanchez, G. Chang, B. Ernst, J. Yin, S. S. Zhang, T. Cochran, N. Shumiya, H. Zheng, *et al.*, Discovery of topological Weyl fermion lines and drumhead surface states in a room temperature magnet, *Science* **365**, 1278 (2019).
- [35] G. Chang, S.-Y. Xu, H. Zheng, B. Singh, C.-H. Hsu, G. Bian, N. Alidoust, I. Belopolski, D. S. Sanchez, S. Zhang, *et al.*, Room-temperature magnetic topological Weyl fermion and nodal line semimetal states in half-metallic Heusler  $\text{Co}_2\text{TiX}$  ( $X = \text{Si, Ge, or Sn}$ ), *Scientific reports* **6**, 1 (2016).
- [36] M. Hirschberger, S. Kushwaha, Z. Wang, Q. Gibson, S. Liang, C. A. Belvin, B. A. Bernevig, R. J. Cava, and N. P. Ong, The chiral anomaly and thermopower of Weyl fermions in the half-Heusler  $\text{GdPtBi}$ , *Nature materials* **15**, 1161 (2016).
- [37] W. Shi, L. Muechler, K. Manna, Y. Zhang, K. Koepnik, R. Car, J. Van Den Brink, C. Felser, and Y. Sun, Prediction of a magnetic Weyl semimetal without spin-orbit coupling and strong anomalous Hall effect in the Heusler compensated ferrimagnet  $\text{Ti}_2\text{MnAl}$ , *Physical Review B* **97**, 060406 (2018).
- [38] R. P. Dulal, B. R. Dahal, A. Forbes, N. Bhattarai, I. L. Pegg, and J. Philip, Weak localization and small anomalous Hall conductivity in ferromagnetic Weyl semimetal  $\text{Co}_2\text{TiGe}$ , *Scientific Reports* **9**, 1 (2019).
- [39] B. Ernst, R. Sahoo, Y. Sun, J. Nayak, L. Muechler, A. K. Nayak, N. Kumar, J. Gayles, A. Markou, G. H. Fecher, *et al.*, Anomalous Hall effect and the role of Berry curvature in  $\text{Co}_2\text{TiSn}$  Heusler films, *Physical Review B* **100**, 054445 (2019).
- [40] S. N. Guin, K. Manna, J. Noky, S. J. Watzman, C. Fu, N. Kumar, W. Schnelle, C. Shekhar, Y. Sun, J. Gooth, *et al.*, Anomalous Nernst effect beyond the magnetization scaling relation in the ferromagnetic Heusler compound  $\text{Co}_2\text{MnGa}$ , *NPG Asia Materials* **11**, 1 (2019).
- [41] J. Noky, Y. Zhang, J. Gooth, C. Felser, and Y. Sun, Giant anomalous Hall and Nernst effect in magnetic cubic Heusler compounds, *npj Computational Materials* **6**, 1 (2020).
- [42] D.-C. Tsai and C.-H. Chiang, Vacuum arc melting processes for biomedical NiTi shape memory alloy, in *MATEC Web of Conferences*, Vol. 30 (EDP Sciences, 2015) p. 01004.
- [43] J. Hafner, Ab-initio simulations of materials using vasp: Density-functional theory and beyond, *Journal of Computational Chemistry* **29**, 2044 (2008).
- [44] P. E. Blöchl, Projector augmented-wave method, *Physical review B* **50**, 17953 (1994).
- [45] G. Pizzi, V. Vitale, R. Arita, S. Blügel, F. Freimuth, G. Géranton, M. Gibertini, D. Gresch, C. Johnson, T. Koretsune, J. Ibañez-Azpiroz, H. Lee, J.-M. Lihm, D. Marchand, A. Marrazzo, Y. Mokrousov, J. I. Mustafa, Y. Nohara, Y. Nomura, L. Paulatto, S. Poncé, T. Ponweiser, J. Qiao, F. Thöle, S. S. Tsirkin, M. Wierzbowska, N. Marzari, D. Vanderbilt, I. Souza, A. A. Mostofi, and J. R. Yates, Wannier90 as a community code: New features and applications, *Journal of Physics: Condensed Matter* **32**, 165902 (2020).
- [46] N. Marzari and D. Vanderbilt, Maximally localized generalized Wannier functions for composite energy bands, *Phys. Rev. B* **56**, 12847 (1997).
- [47] Q. Wu, S. Zhang, H.-F. Song, M. Troyer, and A. A. Soluyanov, Wanniertools: An open-source software package for novel topological materials, *Computer Physics Communications* **224**, 405 (2018).
- [48] M. Gradhand, D. V. Fedorov, F. Pientka, P. Zahn, I. Mertig, and B. L. Györfy, *Journal of Physics: Condensed Matter* **24**, 213202 (2012).
- [49] G. Chang, S.-Y. Xu, H. Zheng, B. Singh, C.-H. Hsu, G. Bian, N. Alidoust, I. Belopolski, D. S. Sanchez, S. Zhang, *et al.*, Room-temperature magnetic topological Weyl fermion and nodal line semimetal states in half-metallic Heusler  $\text{Co}_2\text{TiX}$  ( $X = \text{Si, Ge, or Sn}$ ), *Scientific reports* **6**, 1 (2016).
- [50] J. Rodríguez-Carvajal, An introduction to the program fullprof, Laboratoire Leon Brillouin (CEA-CNRS) (2001).
- [51] Y. Takamura, R. Nakane, and S. Sugahara, Analysis of  $L_{21}$  ordering in full Heusler  $\text{Co}_2\text{FeSi}$  alloy thin films formed by rapid thermal annealing, *Journal of Applied Physics* **105**, 07B109 (2009).
- [52] Y. Sakuraba, K. Hyodo, A. Sakuma, and S. Mitani, Giant anomalous Nernst effect in the  $\text{Co}_2\text{MnAl}_{1-x}\text{Si}_x$  Heusler alloy induced by Fermi level tuning and atomic ordering, *Physical Review B* **101**, 134407 (2020).
- [53] S. Wurmehl, G. H. Fecher, H. C. Kandpal, V. Ksenofontov, C. Felser, and H.-J. Lin, Investigation of  $\text{Co}_2\text{FeSi}$ ,



- the Heusler compound with highest Curie temperature and magnetic moment, *Applied Physics Letters* **88**, 032503 (2006).
- [54] B. Balke, S. Wurmehl, G. H. Fecher, C. Felser, M. d. C. M. Alves, F. Bernardi, and J. Morais, Structural characterization of the  $\text{Co}_2\text{FeZ}$  ( $Z = \text{Al, Si, Ga, and Ge}$ ) Heusler compounds by X-ray diffraction and extended X-ray absorption fine structure spectroscopy, *Applied Physics Letters*. New York. Vol. 90, no. 17 (Apr. 2007), 172501, 3 p. (2007).
- [55] B. Balke, S. Wurmehl, G. H. Fecher, C. Felser, and J. Kübler, Rational design of new materials for spintronics:  $\text{Co}_2\text{FeZ}$  ( $Z = \text{Al, Ga, Si, Ge}$ ), *Science and Technology of advanced Materials* (2008).
- [56] D. Rai, A. Shankar, M. Ghimire, R. Thapa, *et al.*, A comparative study of a Heusler alloy  $\text{Co}_2\text{FeGe}$  using `lsda` and `lsda+u`, *Physica B: Condensed Matter* **407**, 3689 (2012).
- [57] S. Amari, F. Dahmane, S. B. Omran, B. Doumi, I. Yahiaoui, A. Tadjer, and R. Khenata, Theoretical investigation of the structural, magnetic and band structure characteristics of  $\text{Co}_2\text{FeGe}_{1-x}\text{Si}_x$  ( $x = 0, 0.5, 1$ ) full-Heusler alloys, *Journal of the Korean Physical Society* **69**, 1462 (2016).
- [58] D. Goodings, Electrical resistivity of ferromagnetic metals at low temperatures, *Physical Review* **132**, 542 (1963).
- [59] A. Markou, D. Kriegner, J. Gayles, L. Zhang, Y.-C. Chen, B. Ernst, Y.-H. Lai, W. Schnelle, Y.-H. Chu, Y. Sun, *et al.*, Thickness dependence of the anomalous Hall effect in thin films of the topological semimetal  $\text{Co}_2\text{MnGa}$ , *Physical Review B* **100**, 054422 (2019).
- [60] I.-M. Imort, P. Thomas, G. Reiss, and A. Thomas, Anomalous Hall effect in the Co-based Heusler compounds  $\text{Co}_2\text{FeSi}$  and  $\text{Co}_2\text{FeAl}$ , *Journal of Applied Physics* **111**, 07D313 (2012).
- [61] E. V. Vidal, H. Schneider, and G. Jakob, Influence of disorder on anomalous Hall effect for Heusler compounds, *Physical Review B* **83**, 174410 (2011).
- [62] S. Roy, R. Singha, A. Ghosh, A. Pariari, and P. Mandal, Anomalous Hall effect in the half-metallic Heusler compound  $\text{Co}_2\text{TiX}$  ( $X = \text{Si, Ge}$ ), *Physical Review B* **102**, 085147 (2020).
- [63] N. Nagaosa, Anomalous Hall effect-A new perspective, *Journal of the Physical Society of Japan* **75**, 042001 (2006).
- [64] Q. Wang, Y. Xu, R. Lou, Z. Liu, M. Li, Y. Huang, D. Shen, H. Weng, S. Wang, and H. Lei, Large intrinsic anomalous Hall effect in half-metallic ferromagnet  $\text{Co}_3\text{Sn}_2\text{S}_2$  with magnetic Weyl fermions, *Nature communications* **9**, 1 (2018).
- [65] N. Nagaosa, J. Sinova, S. Onoda, A. H. MacDonald, and N. P. Ong, Anomalous Hall effect, *Reviews of Modern Physics* **82**, 1539 (2010).
- [66] I. Campbell and A. Fert, Transport properties of ferromagnets, *Handbook of Ferromagnetic Materials* **3**, 747 (1982).
- [67] Y. Liu, H. Tan, Z. Hu, B. Yan, C. Petrovic, *et al.*, Anomalous Hall effect in the weak-itinerant ferrimagnet  $\text{FeCr}_2\text{Te}_4$ , *Physical Review B* **103**, 045106 (2021).
- [68] D. Liu, A. Liang, E. Liu, Q. Xu, Y. Li, C. Chen, D. Pei, W. Shi, S. Mo, P. Dudin, *et al.*, Magnetic Weyl semimetal phase in a kagome crystal, *Science* **365**, 1282 (2019).
- [69] X. Chen, M. Wang, C. Gu, S. Wang, Y. Zhou, C. An, Y. Zhou, B. Zhang, C. Chen, Y. Yuan, *et al.*, Pressure-tunable large anomalous Hall effect of the ferromagnetic kagome-lattice Weyl semimetal  $\text{Co}_3\text{Sn}_2\text{S}_2$ , *Physical Review B* **100**, 165145 (2019).
- [70] S. V. Faleev, Y. Ferrante, J. Jeong, M. G. Samant, B. Jones, and S. S. Parkin, Unified explanation of chemical ordering, the Slater-Pauling rule, and half-metallicity in full Heusler compounds, *Physical Review B* **95**, 045140 (2017).
- [71] K. R. Kumar, K. K. Bharathi, J. A. Chelvane, S. Venkatesh, G. Markandeyulu, and N. Harishkumar, First-principles calculation and experimental investigations on full Heusler alloy  $\text{Co}_2\text{FeGe}$ , *IEEE Transactions on Magnetics* **45**, 3997 (2009).
- [72] J.-M. Hyun and M. Kim, The half-metallicity of  $\text{Co}_2\text{FeGe}$  full Heusler alloy in (001) thin film: first principles study, *Journal of the Korean Physical Society* **72**, 276 (2018).
- [73] K. Nawa and Y. Miura, Exploring half-metallic Co-based full Heusler alloys using a DFT+U method combined with linear response approach, *RSC advances* **9**, 30462 (2019).
- [74] G. Chang, S.-Y. Xu, X. Zhou, S.-M. Huang, B. Singh, B. Wang, I. Belopolski, J. Yin, S. Zhang, A. Bansil, *et al.*, Topological hopf and chain link semimetal states and their application to  $\text{Co}_2\text{MnGa}$ , *Physical Review Letters* **119**, 156401 (2017).
- [75] D. Xiao, M.-C. Chang, and Q. Niu, Berry phase effects on electronic properties, *Reviews of Modern Physics* **82**, 1959 (2010).